Computing Diffeomorphic Paths with Applications to Cardiac Motion Analysis

Dohyung Seo[1], Jeffrey Ho[2], Jay H. Traverse[3], John Forder[4]
, and Baba C. Vemuri[2]

[1] Department of Electrical and Computer Engineering, University of Florida
[2] Department of Computer and Information Sciences and Engineering
University of Florida
[3] Minneapolis Heart Institute Foundation at Abbott Northwestern Hospital
[4] Department of Biomedical Engineering, University of Florida

Abstract. This paper presents an application of a recently introduced novel framework for computing the diffeomorphic path between two given diffeomorphisms computed from two pairs of image frames in a motion sequence [1]. The specific application we address here is that of cardiac motion analysis. The framework involves a two-step algorithm wherein we first project the given pair of diffeomorphisms onto the space of densities – defined by quotienting out the volume-preserving diffeomorphisms considered as the nuisance parameters and then compute the geodesic path between the two points in this space. The second step lifts the aforementioned geodesic path back into the space of diffeomorphisms. The lifting problem is formulated as a quadratic programming problem with bilinear constraints and solved using the augmented Lagrangian method. Unlike the LDDMM-based techniques, this approach yields a path joining the given pair of diffeomorphisms that becomes a geodesic path upon quotienting out the volume-preserving diffeomorphisms. We use this path as the main feature to discriminate between ischemia patients with and without stem cell treatment. Such a discriminatory power can be very useful in the quantification of differences between controls and patients undergoing the treatment.

1 Introduction

While substantial advances in diagnosis and treatment have been made in the past half century, heart disease unfortunately is still a major cause of morbidity and mortality around the world. Among the novel therapeutic approaches that are currently under active investigation, stem cell-based therapy (e.g., [10]) holds a great promise for the future with revolutionary potential for significant improvement in patient prognosis and disease outlook. This paper proposes an application of a novel computational approach recently introduced in [1] to cardiac motion analysis with the aim of providing clinical researchers image processing tools that can extract subtle and useful features from the MR images for high-level clinical tasks such as patient classification and outcome assessment.

$$(a) \qquad\qquad (b) \qquad\qquad (c) \qquad\qquad (d)$$
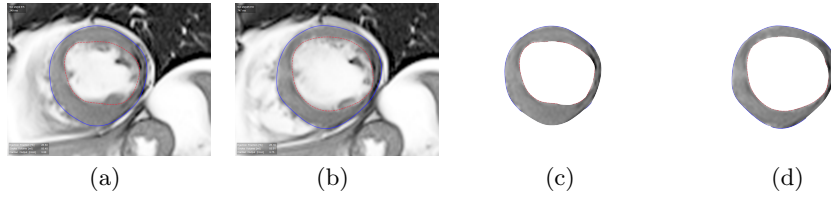
Fig. 1. Top row (a) and (b):the left ventricular myocardium (LVM) at end-systole (ES) and end-diastole (ED). (c) and (d): LVM segmentations of (a) and (b), respectively.

The key idea here is to use smooth paths in the space of diffeomorphisms (of the image domain) as the characterization of the continuous variation in shape and volume of the patient's myocardium across cardiac cycles. More specifically, given a sequence of MR images of a cardiac cycle (Fig.1), we compute a diffeomorphic map between each image and a reference image, the image at the beginning of the cycle. These discretely sampled diffeormorphisms are interpolated to form a smooth path of diffeomorphisms from which useful high-level features can be extracted directly. Unfortunately, the diffeomorphisms are often noisy because the myocardium constantly undergoes small and random movement due to the pressure exerted from its surroundings. While these small random perturbations should be treated as nuisance parameters and modelled with diffeomorphisms close to the identity, there is an important equivalence among them: two small perturbations with the same myocardium volume should have the same clinical significance because it implies the same volume of ejecta in each case. This particular insight naturally leads to the idea of treating volume-preserving diffeomorphisms as the nuisance parameters, and the desired diffeomorphic paths should be smooth paths in an appropriate space that has "taken out" the effects of these nuisance parameters.

The above viewpoint admits a lucid and transparent formulation using the idea of quotient space. Specifically, let Ω denote a 3-D (image) domain with the volume form μ, and $\mathbf{Diff}(\Omega), \mathbf{Diff}(\Omega)_{\mu}$ the infinite-dimensional group of diffeomorphisms of Ω and its infinite-dimensional subgroup of volume-preserving diffeomorphisms, respectively. Mathematically, the quotient space $\mathbf{Diff}(\Omega)/\mathbf{Diff}(\Omega)_{\mu}$ is the space that has factored (taken) out the effect of $\mathbf{Diff}(\Omega)_{\mu}$, and there is a canonical projection map $\mathbf{Diff}(\Omega) \to \mathbf{Diff}(\Omega)/\mathbf{Diff}(\Omega)_{\mu}$. The quotient space has been studied in [6], and it can be identified with the space of density functions $\mathbf{Den}(\Omega)$ on Ω that can be canonically embedded as a convex subset of a sphere in the Hilbert space (See [6] for details). While $\mathbf{Diff}(\Omega)$ is a complicated space, the reduction $\mathbf{Diff}(\Omega) \to \mathbf{Diff}(\Omega)/\mathbf{Diff}(\Omega)_{\mu} = \mathbf{Den}(\Omega)$ provides us with the space $\mathbf{Den}(\Omega)$ of known and computationally tractable geometry. In particular, one straightforward way to exploit this reduction for computing diffeomorphic paths in $\mathbf{Diff}(\Omega)$ is to first compute a geodesic path in $\mathbf{Den}(\Omega)$ and then lift the path back into $\mathbf{Diff}(\Omega)$. Specifically, given the diffeomorphism ρ computed using any registration technique, our method will compute a path in the space of diffeomorphisms connecting ρ with the identity diffeomorphism (see next section for details) using a two-step algorithm that first projects ρ and the
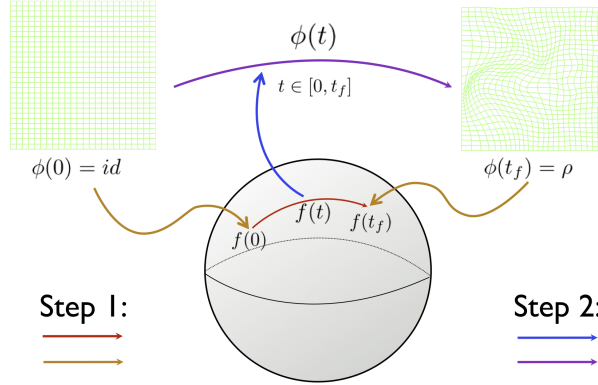
Fig. 2. Illustation of the two main steps in our algorithm for computing diffeomorphic paths. $f(0)$, $f(t_f)$ and $f(t)$ represent projected points of the two given diffeomorphisms and the great circle connecting the two projected points on the sphere, respectively.

identity onto the sphere and computes the unique geodesic joining the two projected points. This is followed by the second step that lifts the geodesic path on the density sphere back to $\mathbf{Diff}(\Omega)$, that is formulated as a quadratic programming problem with bilinear constraints which can be solved using the numerical algorithm proposed in [8] based on the augmented Lagrangian method. While the diffeomorphic path $\phi(t)$ computed by our method is not a geodesic path in $\mathbf{Diff}(\Omega)$, it nevertheless acquires a geodesic interpretation in the sense that by quotienting out the volume-preserving diffeomorphisms, the path $\phi(t)$ is indeed a geodesic path in the quotient space. Fig.2 provides a diagrammatic illustration of this algorithm.

In this paper, we apply our framework to cardiac motion analysis and the classification of ischemia patients. In particular, we show that features extracted from diffeomorphic paths are useful in classifying ischemia patients undergoing stem cell treatment and without treatment. Note that the classification problem does not require us to perform the second step defined above, namely, the lifting step. However, it is the lifting step that explicitly produces an interpolating path between the two given diffeomorphisms, and this step is necessary for visualizing the diffeomorphic path as well as for evaluating the quality of interpolation between the given time sequence of data that are needed in the validation step to assess the accuracy of the computed path.

We structure this paper somewhat differently by first presenting the details of our proposed algorithm and the experimental results on cardiac motion analysis in the following three sections. Related work will be discussed after the presentation of our framework and results, and the discussion will be centered on the relations between our work and that of Large Deformation Diffeomorphic Metric Mapping framework (LDDMM) [2–5] and iDiff framework introduced very recently in [7]. We end this paper with a short conclusion and a plan for future work.

2   Theory and Algorithm

This section presents the aforementioned two-step algorithm for estimating a path of diffeomorphisms connecting a given pair of diffeomorphisms ρ_1, ρ_2. For simplicity of exposition, we will assume that ρ_1 is **id**, the identity diffeomorphism and the necessary modification for general case is straightforward and simply involves a group operation applied to the two diffeomorphisms as $\rho_1^{-1} \circ \rho_1 = \mathbf{id}$ and $\rho = \rho_1^{-1} \circ \rho_2$.

The spaces of densities and diffeomorphisms: Our aim is to compute a diffeomorphic path, $\phi(t)$ between id and ρ such that $\phi(0) = id$ and $\phi(t = t_f) = \rho$ where, $0 \le t \le t_f$, and the image domain Ω will be considered as a compact subset of $\mathbb{R}^3$ with a given volume form $\mu = dxdydz$.

The projection map $\mathbf{\Phi}$ that maps $\mathbf{Diff}(\Omega)$ to the quotient space $\mathbf{Den}(\Omega)$ is given by,

$$\mathbf{\Phi} : \phi \to f = \sqrt{|D\phi|}, \tag{1}$$

where $|D\phi|$ is the determinant of the Jacobian of ϕ with respect to the volume form μ. We note that $\mathbf{\Phi}(\mathbf{id}) = 1$, the constant function one. The space of densities can be identified with an infinite-dimensional sphere of radius $\mu(\Omega)$, the volume of Ω,

$$\int_M \mathbf{\Phi}^2(\phi)d\mu = \mu(\Omega). \tag{2}$$

By scaling $\mathbf{\Phi}$ with $\sqrt{\mu(\Omega)}$, we can further identify $\mathbf{Den}(\Omega)$ with an infinite-dimensional unit sphere. More details are given in [6]. Once the two projected points on the sphere are identified, the unique geodesic path joining the two points f_1, f_2 can be readily determined using the formula [9].

$$f(t) = \frac{1}{\sin(\theta)} \left[\sin(\theta - t) f_1 + \sin(t) f_2 \right], \tag{3}$$

where $f_1 = \sqrt{|D\mathbf{id}|}$, $f_2 = \sqrt{|D\rho|}$, and θ is the angle between the two points on the sphere.

We remark that if the two given diffeomorphisms are already volume-preserving, then by definition, they project to the same point in $\mathbf{Den}(\Omega)$. Hence, their geodesic in $\mathbf{Den}(\Omega)$ is degenerate and consists of just one point, and the lifted diffeomorphic path in $\mathbf{Diff}(\Omega)$ is then a path consisting of only volume-preserving diffeomorphisms.

Given the geodesic path $f(t)$ on $\mathbf{Den}(\Omega)$ and representing diffeomorphic paths using 3-D deformation vector fields, $\phi(t) = (x+U(x, y, z, t), y+V(x, y, z, t), z+W(x, y, z, t))$, the diffeomorphic path $\phi(t) \in \mathbf{Diff}(\Omega)$ is required to satisfy the constraint,

$$\mathbf{\Phi}(\phi(t)) = f(t). \tag{4}$$

Since,

$$|D\phi(t)| = \begin{vmatrix} 1 + U(t)_x & U(t)_y & U(t)_z \\ V(t)_x & 1 + V(t)_y & V(t)_z \\ W(t)_x & W(t)_y & 1 + W(t)_z \end{vmatrix}, \tag{5}$$

we have

$$f(t)^2 = |D\phi(t)|/\mu(\Omega). \tag{6}$$

Eq.(5) gives the determinant of the Jacobian of ϕ, and $U(t)_i$, $V(t)_i$, and $W(t)_i$ denote the first-order derivatives with respect to $i \in \{x, y, z\}$. Our next step is to recover the deformation fields, $\phi(t)$ from Eq.(6). We remark that the proposed method does not explicitly perform spatial regularization on diffeomorphic paths, Instead, the diffeomorphic paths will be computed by lifting using the Jacobian constraints.

Path Lifting: The constraint provided by Eq.(6) does not determine a unique solution, and geometrically, this corresponds to the fact that Eq.(6) only requires $\phi(t)$ to lie on a $\mathbf{Diff}(\Omega)_\mu$-orbit in $\mathbf{Diff}(\Omega)$ parameterized by the point $f(t)$ in the sphere. Therefore, we will compute the lifted path in $\mathbf{Diff}(\Omega)$ using L^2-based regularization: L^2 smoothness of the deformation vector fields over time as the main regularization criterion. We note that while other regularization schemes are possible, e.g., using the Sobolev norm, we have chosen the L^2 regularization because of its computational simplicity. This leads to the following quadratic programming problem with bilinear constraints:

$$\min \int \left| \frac{dU(x,y,z,t)}{dt} \right|^2 + \left| \frac{dV(x,y,z,t)}{dt} \right|^2 + \left| \frac{dW(x,y,z,t)}{dt} \right|^2 d\mu dt$$
$$s.t. \quad |D\phi(t)| = f(t)^2 \mu(\Omega). \tag{7}$$

We remark that the continuity of the computed diffeomorphic path is always assured because its projection on the sphere is a continuous path (in fact, a smooth geodesic path). Specifically, the domain of the optimization problem specified in Equation 7 can be taken to be the set $\mathcal{C}$ of all C^1-diffeomorphic paths[5] that project to the given geodesic on the sphere (i.e., satisfying the constraint Equation 4). The set $\mathcal{C}$ is nonempty because of the connectedness of both the fiber (the group of volume-preserving diffeomorphisms) and the base curve (the geodesic path on sphere). We also note that our diffeomorphic path is always computed for two given diffeomorphisms (**id** and ρ defined above) and not among several diffeomorphisms.

---

[5] Or some suitable completion of the set of all C^1-diffeomorphic paths under an appropriate Soblev norm.

3   Optimization

While Eq.(7) is formulated for continuous variables x, y, z and t, in practice, we have to work with discrete pixels and time, and its discrete version is given by,

$$
\min_{U_{ijk}^t, V_{ijk}^t, W_{ijk}^t} \sum_{i,j,k,t} \left[\left| \frac{U_{ijk}^{t+1} - U_{ijk}^{t-1}}{2\delta x} \right|^2 + \left| \frac{V_{ijk}^{t+1} - V_{ijk}^{t-1}}{2\delta y} \right|^2 + \left| \frac{W_{ijk}^{t+1} - W_{ijk}^{t-1}}{2\delta z} \right|^2 \right] \delta t \delta x \delta y \delta z
$$

$$
s.t. \quad \begin{vmatrix} 1 + U_{x_{ijk}}^t & U_{y_{ijk}}^t & U(t)_{z_{ijk}}^t \\ V_{x_{ijk}}^t & 1 + V_{y_{ijk}}^t & V_{z_{ijk}}^t \\ W_{x_{ijk}}^t & W_{y_{ijk}}^t & 1 + W_{z_{ijk}}^t \end{vmatrix} - \mu(\Omega)(f_{ijk}^t)^2 = 0,
$$

(8)

where the superscript t and subscript i, j, k denote the discrete time and voxel indices respectively, and the subscripts x, y and z in the constraints denote the first-order derivatives w.r.t. x, y and z respectively. We set δx, δy and δz to be one, and therefore the volume $\mu(\Omega)$ is the image size.

Geometrically, the determinant of the Jacobian $|D\phi(t)|$ is the ratio of the change of volume elements by $\phi(t)$ at domain points and time t. In our numerical scheme, $|D\phi(t)|$ is formulated as the volume of a hexahedral cell composed with six-neighbour voxels which are displaced by the deformation vector fields. This 3-D formulation is adopted in Eq.(1) as well, and efficient ways to compute the volume are discussed in [11]. In [1], $|D\phi(t)|$ in 2-D was formulated as a quadrilateral composed with four neighbouring pixels, and the optimization problem was formulated as a quadratic programming problem with bilinear constraints. Now, in this 3-D problem, the formulation leads to the same optimization problem but with trilinear constraints: As shown in [12], considering $|D\phi(t)|$ to be the volume of a hexahedral cell and vectorizing all deformation vector fields, the optimization problem is formulated explicitly as follows:

$$
\min \frac{1}{2}\mathbf{U}^\mathsf{T}\mathbf{R}\mathbf{U} + \frac{1}{2}\mathbf{V}^\mathsf{T}\mathbf{R}\mathbf{V} + \frac{1}{2}\mathbf{W}^\mathsf{T}\mathbf{R}\mathbf{W} + \mathbf{B}_u^\mathsf{T}\mathbf{U} + \mathbf{B}_v^\mathsf{T}\mathbf{V} + \mathbf{B}_w^\mathsf{T}\mathbf{W}
$$

$$
s.t. \ \mathbf{h} = \mathbf{c} + \mathbf{C}_V\mathbf{V} + \mathbf{C}_W\mathbf{W} + (\mathbf{C}_U + \mathbf{D}_U(\mathbf{V}) + \mathbf{D}_U(\mathbf{W}) + \mathbf{E}_U(\mathbf{V},\mathbf{W}))\mathbf{U} = 0
$$

$$
or \ \mathbf{h} = \mathbf{c} + \mathbf{C}_U\mathbf{U} + \mathbf{C}_W\mathbf{W} + (\mathbf{C}_V + \mathbf{D}_V(\mathbf{U}) + \mathbf{D}_V(\mathbf{W}) + \mathbf{E}_V(\mathbf{U},\mathbf{W}))\mathbf{V} = 0
$$

$$
or \ \mathbf{h} = \mathbf{c} + \mathbf{C}_U\mathbf{U} + \mathbf{C}_V\mathbf{V} + (\mathbf{C}_W + \mathbf{D}_W(\mathbf{U}) + \mathbf{D}_W(\mathbf{V}) + \mathbf{E}_W(\mathbf{U},\mathbf{V}))\mathbf{W} = 0,
$$

(9)

Let us suppose that the size of domain is $M \times N \times L$. Then, in the above, $\mathbf{U}^\mathsf{T} = (\mathbf{U}^\mathsf{T}(t = 2), ..., \mathbf{U}^\mathsf{T}(t = T - 1))$, and $\mathbf{B}_u^\mathsf{T} = (\mathbf{U}^\mathsf{T}(t = 1), \mathbf{0}^\mathsf{T}, \mathbf{U}^\mathsf{T}(t = T))$ where $\mathbf{0}$ is a vector of zeros with length $M \times N \times L \times (T - 4)$ if we have a time sequence $t \in [1, T]$ including two boundary conditions namely, $\phi(0) = id$ and $\phi(T) = \rho$. $\mathbf{V}$ ($\mathbf{W}$) and $\mathbf{B}_v$ ($\mathbf{B}_w$) are defined in the same way. In Eq.(9), $\mathbf{R}$ is the matrix for the quadratic component and its size is $M \times N \times L \times (T - 2)$. $\mathbf{C}_U\mathbf{U}$, $\mathbf{C}_V\mathbf{V}$ and $\mathbf{C}_W\mathbf{W}$ correspond to the linear terms of $\mathbf{U}$, $\mathbf{V}$ and $\mathbf{V}$ in the volume formulation of the hexahedral cells, respectively. $\mathbf{D}$'s and $\mathbf{E}$'s correspond to the bilinear and trilinear terms after factoring out $\mathbf{U}$, $\mathbf{V}$ and $\mathbf{W}$, respectively. Finally, $\mathbf{c}$ is the vectorization of $\mu(\Omega)(f_{ijk}^t)^2$ in Eq.(8) plus a vector of ones and $\mu(\Omega) = (M - 1)(N - 1)(L - 1)$. More details are provided in Appendix E of [12]

We solve the optimization using the augmented Lagrangian method with penalty [8] by iteratively solving for the three blocks of variables $\mathbf{U}, \mathbf{V}, \mathbf{W}$, fixing

two of these while optimizing the rest. For instance, with fixed $\mathbf{V}$ and $\mathbf{W}$, the problem is given by,

$$\min \frac{1}{2}\mathbf{U}^\mathsf{T}\mathbf{R}\mathbf{U} + \mathbf{B}_u^\mathsf{T}\mathbf{U} + \lambda^\mathsf{T}\mathbf{h} + \frac{1}{2}c||\mathbf{h}||^2$$
$$s.t. \quad \mathbf{U} \in \mathbb{R}^m,$$

(10)

where, $\lambda \in \mathbb{R}^m$ is the Lagrange multiplier, $c \to \infty$ and $m = M \times N \times L \times (T-2)$. This is an unconstrained optimization problem and can be rewritten more clearly as,

$$\min \frac{1}{2}\mathbf{U}^\mathsf{T}(\mathbf{R} + c\mathbf{H}_u^\mathsf{T}\mathbf{H}_u)\mathbf{U} + (\mathbf{B}_u + \frac{1}{2}c((\mathbf{G}_u^\mathsf{T}\mathbf{H}_u)^\mathsf{T} + \mathbf{H}_u^\mathsf{T}\mathbf{G}_u) + (\lambda^\mathsf{T}\mathbf{H}_u)^\mathsf{T})^\mathsf{T}\mathbf{U}$$
$$s.t. \quad \mathbf{U} \in \mathbb{R}^m,$$

(11)

where, $\mathbf{H}_u = \mathbf{C}_U + \mathbf{D}_U(\mathbf{V}) + \mathbf{D}_U(\mathbf{W}) + \mathbf{E}_U$ and $\mathbf{G}_u = \mathbf{c} + \mathbf{C}_V\mathbf{V} + \mathbf{C}_W\mathbf{W}$. That is, $\mathbf{h} = \mathbf{H}_u\mathbf{U} + \mathbf{G}_u$.

4 Experiments

We have acquired cardiac MR scans of patients with acute myocardial infraction (AMI), and they were randomized into one of two groups: control and treatment. The treatment group received endothelial progenitor stem cell (EPCs) treatment, while the control received a cell-free infusion. Cardiac MRI exams were performed at baseline which was prior to EPC therapy, and following six months post-treatment [10]. Generally, cardiac analysis involves measuring the average wall motion, or wall thickening reported for each of the individual segments of hearts. We propose a patient classification method (between control and treatment groups) by measuring changes of diffeomorphic paths over six months. These diffeomorphic paths are the diastolic filling motion of the left ventricular myocardium (LVM) computed using our method. For the experiments, we have expert-segmented LVM's from the cardiac MR scans, and examples of LVM and its segmentation are shown in Fig.1.

Data Acquisition: The cardiac data was acquired along the short-axis of the heart using a cine multislice sequence using a Siemens Avanto 1.5T whole body MRI scanner. Twenty-five phases were collected throughout the cardiac cycle using a TrueFISP (a balanced coherent gradient sequence using Fast Imaging with Steady state free Precession), with an echo time of 1.13ms and an apparent repetition time of 71.82ms. Data was collected using a total of 161 phases encoded into a matrix of 256×151, yielding an in-plane resolution of 1.71875×1.71875mm^2. Slice thickness was 7mm, with a slice separation of 10mm. Coverage of the myocardium extended from above the valve plane at the base, to below the apex throughout the cardiac cycle.

In the first experiment, we compare the interpolated paths between end-systole (ES) and end-diastole (ED) using our method and LDDMM, given the ground truth. For this comparison, we choose eighteen intermediate time points
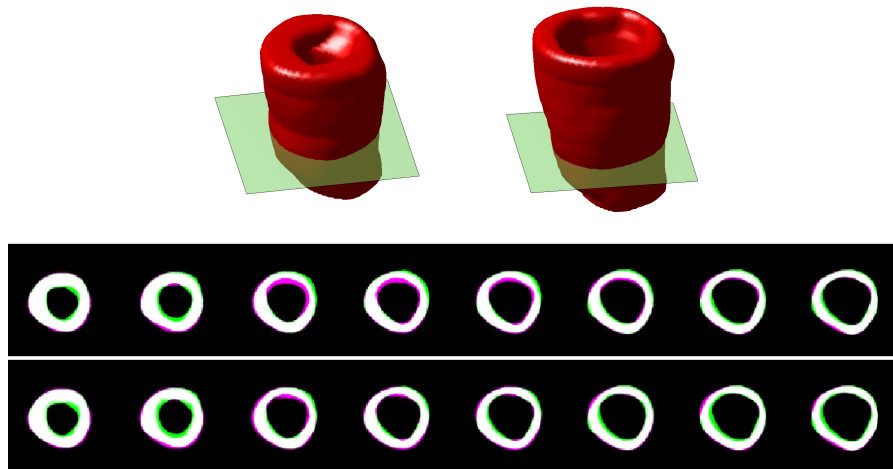
Fig. 3. Comparison between the ground truth and estimated temporal changes of the cardiac chamber from ES to ED along the short-axis in 3-D. A 2-D slice shown in green color plane is chosen to depict the changes over the cardiac cycle in the bottom two rows. Top: 3-D shapes of LVM at ES (left) and ED (right). Middle and bottom: computed changes using LDDMM and our method respectively. The white region represents the intersection of the ground truth and estimates, and green and magenta represent voxels belonging to the ground truth and estimates respectively.

along the interpolated path at which the comparison is performed. This comparison is repeated for five different patients. A visual comparison is provided in Fig,3. The images in the top row in Fig.3 represent 3-D shapes of LVM at ES (left) and ED (right). For visual comparison, first, we choose a short-axis which is presented as green planes in the top images and compare the ground truth of the temporal change of this 2-D slice (from 3-D) with computed ones using LDDMM and our method respectively. The middle and bottom rows in Fig.3 show the results from LDDMM and our method respectively. The white region represents the intersection of the ground truth and estimates from the applied algorithm, and green and magenta represent voxels which belong to the ground truth and estimates. It is hard to tell which method estimates the ground truth with higher quality (even though we can recognize that in the middle frames the shapes from our method fit better to the ground truth than the ones from LDDMM). However, quantitative comparison shows clear difference between our method and LDDMM: We report the Dice coefficients between the ground truth and the interpolated LVM images obtained using our method and the LDDMM method. The results tabulated in Table 1 show that the proposed method outperforms LDDMM using the Dice coefficient as the evaluation metric.

Ischemia Patient Classification: In the second experiment, we classify the two groups of ischemia patients described in the previous sections. The stem-cell therapy used in the treated patient group is supposed to improve the diastolic filling motion of the left ventricular myocardium (LVM); therefore, an approach

Table 1. The Dice coefficients of the estimated intermediate cardiac frames using our method and the LDDMM.

	Average	Median	Variance
Our method	0.912	0.908	0.0009
LDDMM	0.901	0.897	0.0018

for classification between the two groups is to measure how the diastolic filling motion of LVM changes over six months with/without EPC therapy. The cycle of LVM diastolic filling motion is from end-systole (ES) to end-diastole (ED), and we take the images of segmented LVM at ES and ED as the I_s's and I_t's. We then compute the diffeomorphic path $\phi(t)$ of nine subjects in the control group and 21 in the treated group, and all paths have ten intermediate time points between ES and ED. Next, we express $U(t), V(t)$, and $W(t)$ of $\phi(t) = (x+U(t), y+V(t), z+W(t))$ in a discrete sine and cosine (DSC) basis. We collect all the DSC coefficients of U, V and W into a single vector for each patient, and the motion change of LVM over six months for each patient is measured using the L_2 distance of DSC coefficients between baseline scan and 6-months scan. We use this as the feature for classification. In this experiment, we use the Support Vector Machine (SVM) as the classifier with polynomial kernel of degree three. The number of DSC basis elements for each component of $\phi(t)$ is five, and we use a leave-one-out cross validation. Table 2 shows the classification results using our method and LDDMM, and it is evident that our method significantly outperforms LDDMM. Note that the LDDMM-based method results in lower classification rates because of the inherent hard parameter selection problem associated with it. In contrast, our method does not have any such parameter selection issue as evident from our quadratic programming formulation.

Table 2. Classification scores using Support Vector Machine

	Classification score			
Validation method	The proposed method		LDDMM	
	Control	Treatment	Control	Treatment
Leave-one-out	77.78%	85.71%	66.67%	69.56%

5 Discussion

One of the most intensively studied frameworks for computing diffeomorphic path is the Large Deformation Differomorphic Metric Mapping framework (LDDMM) [2–5]. In LDDMM, the diffeomorphic path ϕ is obtained by solving the following equation

$$\frac{d}{dt}\phi(t, \cdot) = v(t, \phi(t, \cdot)), \tag{12}$$

where $v(t, \cdot)$ is a time-varying velocity field defined on Ω. For computing a diffeomorphic path joining two diffeomorphisms (e.g., **id** and ρ), ϕ is required to satisfy

the boundary condition $\phi(1, \cdot) = \rho$. In the registration context, LDDMM's objective function almost always has two terms: the data term that matches images and the regularization term that is based on the magnitude of the time-varying vector field v measured in an appropriate norm. Therefore, the objective function requires at least one coupling constant to modulate the contributions of the two terms. In contrast, our method detaches the registration process from the process that computes the diffeomorphic path. Consequently, it does not require a coupling constant whose determination is often highly nontrivial, and the experimental comparisons presented above can be partially attributed to the (potentially) non-optimal coupling constants used for LDDMM. Furthermore, it is also highly nontrivial to modify the LDDMM framework for minimizing the effect of volume-preserving diffeomorphisms (as nuisance parameters). In fact, the diffeomoprhic paths computed by LDDMM and our method are generally different, and projecting LDDMM's diffeomorphic path onto the quotient space $\mathbf{Diff}(\Omega)/\mathbf{Diff}(\Omega)_\mu$ in general does not produce a geodesic on $\mathbf{Den}(\Omega)$. The inability of LDDMM to deal with the nuisance parameters at least in part explains the difference in classification performance reported in Table 2.

The space of diffeomorphisms $\mathbf{Diff}(\Omega)$ is infinite-dimensional, which readily explains the difficulty of computing diffeomorphic paths. Using the projection map $\mathbf{\Phi}$ (Equation 1), the tangent space of $\mathbf{Diff}(\Omega)$ at ρ has the following natural decomposition (given a Riemannian metric on $\mathbf{Diff}(\Omega)$)

$$\mathbf{T}_\rho\mathbf{Diff}(\Omega) = \mathbf{T_{id}Diff}(\Omega)_\mu \oplus \mathbf{T}_{\mathbf{\Phi}(\rho)}\mathbf{Den}(\Omega), \qquad (13)$$

where $\mathbf{T_{id}Diff}(\Omega)_\mu$ is the tangent space of $\mathbf{Diff}(\Omega)_\mu$ at the identity $\mathbf{id}$ and $\mathbf{T}_{\mathbf{\Phi}(\rho)}\mathbf{Den}(\Omega)$ is the tangent space of $\mathbf{Den}(\Omega)$ at $\mathbf{\Phi}(\rho)$. Direct minimization of the norm of the time-dependent velocity field v as in LDDMM requires considering the entire tangent space $\mathbf{T}_\rho\mathbf{Diff}(\Omega)$, and it is often fraught with problems, not the least because there are no guarantees on the quality of the solution. Compared with LDDMM, the minimization specified in Equation 7 requires only $\mathbf{T_{id}Diff}(\Omega)_\mu$-component as the $\mathbf{T}_{\mathbf{\Phi}(\rho)}\mathbf{Den}(\Omega)$-component is fixed by the Jacobian constraint. Therefore, our method reduces the dimension by half, and although still infinite-dimensional, the reduction provides a more restricted domain for optimization that can be easier to analyze and optimize.

Recently, after submitting our work, we were made aware of a novel framework that shares a significant conceptual similarity with ours. The paper [7] introduces the notion of irrotational diffeomorphisms $\mathbf{iDiff}$ based on Brenier's polar factorization theorem for diffeomorphisms: an arbitrary diffeormorphism $\varphi = S \circ \psi$ in $\mathbb{R}^n$ can be uniquely factorized as the composition of a volume-preserving diffeomorphism S and an irrotational diffeomorphism $\psi \in \mathbf{iDiff}(\mathbb{R}^n)$. In particular, $|D\varphi| = |D\psi|$, and $\mathbf{\Phi}(\varphi) = \mathbf{\Phi}(\psi)$. Using the language of quotient space, the result in [7] can be interpreted as an explicit construction of a section of the projection $\mathbf{\Phi}$ in Equation 1. In other words, the projection map $\mathbf{\Phi}$ restricted to the irrotational diffeomorphisms $\mathbf{iDiff}$ is bijective onto the image of $\mathbf{\Phi}$. With this interpretation, the appearance of the square-root of the deter-

minant of the Jacobian in the following main formula (Equation 17 in [7])

$$P : \mathbf{iDiff}(\mathbb{R}^d) \to L^2(\mathbb{R}^d) \ , \ P(\psi) = 2\sqrt{|D\psi| - 1} = 2(\mathbf{\Phi}(\psi) - 1) \qquad (14)$$

becomes less surprising. Furthermore, at tangent space-level, the factorization corresponds to the Helmholtz-Hodge decomposition of the vector fields that decompose the tangent space $\mathbf{T_{id}Diff}(\Omega)$ as the direct sum of divergence-free vector fields and their orthogonal complement, which corresponds to the decomposition in Equation 13 above with $\mathbf{T_{id}Diff}(\Omega)_\mu$ identified with divergence-free vector fields. However, an important and subtle difference is that [7] works with diffeomorphisms on $\mathbb{R}^n$ with compact support while we work with diffeomorphisms on a connected compact domain in $\mathbb{R}^n$. The compactness of the domain implies that it has finite volume, and this translates into the fact that the image of $\mathbf{\Phi}$ is on a sphere of finite radius (Equation 2) with nonzero curvature. The above map $P : \mathbf{iDiff}(\mathbb{R}^d) \to L^2(\mathbb{R}^d)$ can be interpreted geometrically as spherical chords centered at $\mathbf{\Phi}(\mathbf{id})$, and due to the curvature of the sphere, the image of P is never an open neighborhood of zero in $L^2(\mathbb{R}^d)$ when the domain has finite volume. However, the flatness result in [7] can be readily seen (as a limit) from the following heuristic argument[6].

Let $n = 2$ and $D_1 \subset D_2 \subset ... \subset \mathbb{R}^2$ denote a nested sequence of domains where $D_k = \{(x, y) \in \mathbb{R}^2 \| \ |x| \le k, |y| \le k \}$. Each pair $(D_k, \mu), k = 1, 2, ...$ is a compact domain in $\mathbb{R}^2$ with area (volume) $4k^2$. Correspondingly, we will denote $\mathbf{iDiff}_1 \subset \mathbf{iDiff}_2... \subset \mathbf{iDiff}(\mathbb{R}^2)$ the nested sequence of subsets of $\mathbf{iDiff}(\mathbb{R}^2)$, where $\mathbf{iDiff}_n$ contains irrotational diffeomorphisms with support in D_n. The set of irrotational diffeomorphisms with compact support is then the union of $\mathbf{iDiff}_n$:

$$\mathbf{iDiff}(\mathbb{R}^2) = \bigcup_{n=1}^{\infty} \mathbf{iDiff}_n.$$

Therefore, under the projection map $\mathbf{\Phi}$, $\mathbf{iDiff}_k$ maps to a convex set on the sphere of radius $4k^2$. Recall that the curvature of a sphere with radius $4k^2$ is $\frac{1}{4k^2}$, and this shows that as $k \to \infty$, $\mathbf{\Phi}$ maps $\mathbf{iDiff}(\mathbb{R}^2)$ to a sphere with infinite radius, i.e., a space with zero curvature.

6   Conclusions

In this paper, we have applied the novel framework introduced in [1] for computing a diffeomorphic path interpolating two given diffeomorphisms from a cardiac cycle. We have argued that the volume-preserving diffeomorphisms should be considered as nuisance parameters, and clinically relevant diffeomorphic paths should be induced from smooth paths in the corresponding quotient space, taking out the effect of the nuisance parameters. The diffeomorphic path computed by our method enjoys the property that its projection onto the quotient space is indeed a geodesic. The proposed algorithm has two main steps. First, it projects

---

[6] A more detailed comparison of these two approaches will be presented in a forthcoming paper

the two given diffeomorphisms computed from any image registration process onto the quotient space that has been shown to be a convex subset of the infinite-dimensional sphere, and it computes the geodesic between these two projected points in closed form. Second, it lifts this geodesic path on the sphere back to the space of diffeomorphisms using an L_2-regularization that results in a quadratic programming problem with trilinear constraints for 3-D problems that can be efficiently solved using the augmented Lagranigian method.

We have applied our algorithm to two cardiac motion analysis experiments. In the first experiment, the result has shown that the proposed method performs better than LDDMM in estimating the diffeomorphic path between end-systole (ES) and end-diastole (ED). The result from the second experiment has demonstrated the features extracted from the diffeomorphic paths are relevant and useful for patient classification (treated and untreated groups). Our future research will focus on developing more statistical analysis methods in the quotient space described in this paper.

References

1. Seo, D., Ho, J., Vemuri, B.C.: Computing Diffeomorphic Paths for Large Motion Interpolation. *Proc.* CVPR, 1227-1232, (2013).
2. L. Younes: Shapes and Diffeomorphisms. Springer, Heidelberg (2010).
3. Beg, M.F., Miller, M.I., Trouv, A., Younes, L.: Computing Large Deformation Metric Mappings vis Geodesic Flows of Diffeomorphisms. IJCV **61**(2), 139-157, (2005).
4. Younes, L., Arrate, F., Miller, M.I.: Evolutions Equations in Computational Anatomy. Neuroimages, 45, 40-50, (2009).
5. Sommer, S., Nielsen, M., Lauze, F., Pennec, X.: A Multi-scale Kernel Bundle for LDDMM: Towards Sparse Deformation Description Across Space and Scales. IPMI 2011, LNCS, vol. 6081, pp. 624-635, (2011).
6. Khesin, B., Lenells, J., Misiolek, G., Preston, S.C.: Geometry of Diffeomorphism Groups, Complete Integrability and Geometric Statistics. arXiv:1105.0643 (2011).
7. Hinkle, J., Joshi, S.: IDiff: Irrotational Diffeomorphisms for Computational Anatomy. In: Proc. IMPI, 754-765, (2013).
8. Carotenuto, L., Raiconi, G.: On the Minimization of Quadratic Functions with Bilinear Constraints via Augmented Lagrangians. Journal of optimization theory and applications, **55**, 1, 23-36, (Oct. 1987).
9. Srivastava, A., Jermyn, I., Joshi, S.H.: Riemannian Analysis of Probability Density Functions with Application in Vision. In: Proc. CVPR, 18-23, (2007).
10. Petersen, J.W., Forder, J.R., Thomas, J.D., Moye, L.A., Lawson, M., Loghin, C., Traverse, J.H., Baraniuk, S., Silva, G., Pepine, C.J.: Quantification of Myocardial Segmental Function in Acute and Chronic Ischemic Heart Disease and Implications for Cardiovascular Cell Therapy Trials: a Review from the NHLBI-Cardiovascular Cell Therapy Research Network, JACC Cardiovasc Imaging, **4**(6), 71-9, (2011).
11. Grandy, J.: Efficient computation of volume of hexaheral cells, No. UCRL-ID-128886, Lawrence Livermore National Lab., CA (United States), (1997).
12. Seo, D.: A Geometric Approach to Image Matching and Synthesis of Diffeomorphic Paths. Ph.D dissertation, University of Florida, (2013).